Catalysis Science & Technology

Accepted Manuscript

ROYAL SOCIETY OF CHEMISTRY

www.rsc.org/catalysis

Journal Name

RSCPublishing

ARTICLE

Cite this: DOI: 10.1039/x0xx00000x

Fe_3O_4@TiO_2 preparation and catalytic activity in heterogeneous photocatalytic and ozonation processes

Received ooth January 2012,
Accepted ooth January 2012

DOI: 10.1039/x0xx00000x

www.rsc.org/

L. Ciccotti[a], L.A.S. do Vale[a,b], T.L.R. Hewer[a,c] and R.S. Freire[a]*

Several experimental variables were systematically evaluated in the preparation of Fe_3O_4 magnetic nanoparticles. The influence of the preparation parameters on the hydrodynamic diameter and size distribution was examined. The studied experimental parameters include reaction temperature, ultrasonic bath time, stirring speed/time, base concentration/addition rate and stabilizer percentage/stirring time. Depending on experimental conditions, materials with an average size ranging between 11 nm and 35 nm were obtained. The Fe_3O_4 magnetic nanomaterial was used to prepare the hybrid catalyst Fe_3O_4@TiO_2. The prepared materials were characterized by X-ray diffraction, field-emission scanning electron microscopy, transmission electron microscopy, Fourier transform infrared spectroscopy, thermogravimetric and differential thermal analysis, inductively coupled plasma optical emission spectrometry, BET specific surface area and dynamic light scattering. Fe_3O_4@TiO_2 was employed in the degradation of the major metabolite of dipyrone, 4-methylaminoantipyrine, by heterogeneous photocatalytic and ozonation processes. The hybrid material exhibited catalytic activity in both processes.

Introduction

Advanced oxidation processes (AOP) represent efficient treatments for the removal of refractory pollutants in water. Heterogeneous catalytic ozonation and heterogeneous photocatalysis are among the most investigated AOP. In these processes, catalysts are usually employed in suspension or are immobilized over support matrices. When using the catalyst in suspension, it is necessary to separate it from the medium after treatment, adding a time-consuming, laborious and expensive step. On the other hand, immobilization usually reduces the accessible catalyst surface and hence reduces catalytic activity. Magnetic nanoparticles have been extensively studied as a support for many hybrid materials [1, 2]. Fe_3O_4 magnetic proprieties allow effective and easy separation from the reaction media by applying an external magnetic field. Moreover, nanosized magnetic particles have very large specific surface areas, which can be functionalized in order to produce hybrid materials with tailored properties. Titanium dioxide is by far the most common catalyst in photocatalysis due to its electronic properties, chemical stability, non-toxicity and low cost [3-7]. TiO_2 can also be used in heterogeneous catalytic ozonation processes or in combined processes [8-10]. Several studies have reported the use of magnetic catalysts with core-shell configurations in which the core consists of magnetic particles (such as Fe_3O_4) and the surface of catalytically active particles (TiO_2, for example) [11-13]. These materials can be easily separated from the treated water and/or wastewater under the application of an external magnetic field. Thus, functionalized magnetic nanoparticles can be an effective catalyst for oxidative treatment of different pollutants.

Dipyrone is an analgesic broadly used in Brazil [14] and many other countries [15]. Dipyrone is easily hydrolyzed into 4-methylaminoantipyrine (4-MAA) [16-18]. This and other dipyrone metabolites are not completely eliminated by biological treatment, and although little is known about their behavior and persistence in the environment, they have already been detected in surface water at high concentrations [15, 18, 19].

In this paper, the preparation of Fe_3O_4 magnetic nanoparticles under different experimental conditions and the effect on the particle hydrodynamic diameter and size distribution were evaluated. The magnetic nanoparticles were used to prepare the hybrid catalyst Fe_3O_4@TiO_2. This material was applied in the degradation of 4-MAA, the major dipyrone metabolite, by heterogeneous catalytic ozonation and photocatalysis treatment processes.

Materials and methods

Preparation of magnetic nanoparticles

Magnetic nanoparticles were prepared by the co-precipitation method. $FeCl_3.6H_2O$ and $FeCl_2.4H_2O$ (Aldrich) were dissolved in HCl 2 mol L^{-1} to obtain solutions with concentrations of 1 mol L^{-1} Fe(III) and 2 mol L^{-1} Fe(II). A 4 mL volume of Fe(III) solution and 1 mL of Fe(II) solution were mixed, followed by 50 mL of ammonium hydroxide solution. The mixture was stirred for different times (base concentration and precipitation reaction stirring time were varied as described in Table 1 and 2) [11, 20-24]. After complete precipitation, the solid was separated from the solution by magnetic decantation and then washed several times with deionized water. In a subsequent step, 25 mL of tetramethylammonium hydroxide (TMA) solution

was added to the magnetic precipitate (stabilizer concentration was varied as described in Tables 1 and 2) [20, 25]. These dispersions were stirred for different periods of time (Tables 1 and 2). Nitrogen gas was passed continuously through the reaction system. The particles were washed and redispersed in deionized water.

The conditions for magnetic nanoparticles synthesis were modulated by "ANOVA Factorial Design". This statistical design consists of selecting a small number of representative experiments within the experimental domain of interest to study the influence of the process variables (called factors) on the output variables (called responses). Factors are the independent variables of interest, and levels are the experimental conditions related to a given factor. This statistical design has the ability to select samples with high representativeness within the experimental domain used and allows working at various variable levels [26-29]. Based on the results of individual factor trials, a minimal number of experiments were calculated using the STATISTICA 10.1 software (StatSoft Inc., USA).

These chosen variables (factors) and their value ranges are presented in Table 1. Table 2 describes nine different values chosen for each factor. The combination of variables values in each experiment and the order in which the experiments were performed were randomly chosen. Hydrodynamic diameters and their respective distribution were the response variables.

Table 1. Experimental factors settings for Fe_3O_4 nanoparticles preparation.

Factors	Parameters	Units	Range
F1	temperature	°C	5 – 45
F2	precipitation reaction stirring time	min	15 – 135
F3	sonication time	min	15 – 63
F4	precipitation reaction stirring speed	rpm	400 – 2000
F5	base addition rate	mL min^{-1}	0.5 – 2.1
F6	dispersion stirring time	min	2.5 – 10.5
F7	base concentration	mol L^{-1}	0.400 – 1.000
F8	stabilizer percentage	m m^{-1}	1.0 – 3.4

The magnetic material obtained under optimized conditions was used to prepare the hybrid catalyst Fe_3O_4@TiO_2. TiO_2 nanoparticles were prepared by the sol-gel method. Titanium n-butoxide, 33 mL, was added dropwise under vigorous stirring to 200 mL of an aqueous nitric acid solution at 50 °C. The reaction solution was maintained under stirring until peptization was completed and a transparent solution was achieved [30]. In the Fe_3O_4@TiO_2 catalyst preparation, TiO_2 and Fe_3O_4 ratio was 2:1 (weight). Thus, 200 mL of TiO_2 sol were added to 357 mL of magnetite suspension and stirred for 3 hours. The resulting catalyst was dried at 70 ºC and thermally treated under air at 300 ºC for 1 hour.

Characterization

Thermogravimetric (TG) and differential thermal analysis (DTA) curves were obtained with a Shimadzu TGA-50 using a platinum crucible with a sample mass of 10 mg. The heating rate was 10 ºC min^{-1}, between 25 and 1000 ºC, in nitrogen atmosphere (50 mL min^{-1}).

Infrared spectra were recorded on a Shimadzu IR Prestige-21 spectrophotometer between 400 and 4000 cm^{-1}. Spectra were obtained after 20 accumulations, with a resolution of 1 cm^{-1}.

Nitrogen adsorption measurements were conducted at −196 ºC using a Quantachrome volumetric adsorption analyzer, model 100E. Surface areas were determined according to the standard Brunauer, Emmet and Teller (BET) method [31]. Volume and pore radii were determined by the numerical integration method of Barrett, Joyner and Halenda (BJH) [32] and Density Functional Theory (DFT) [33].

Scanning electron microscopy (SEM) studies were performed with a JEOL SEM-FEG JSM-7410 microscope, operated at an accelerating voltage of 1.0 kV and with an LEI and SEI detector. A few droplets of a sample suspended in water were placed on a silicon wafer and dried in a vacuum at 70ºC for 12 hours. Transmission electron microscopy (TEM) studies were conducted using a TEM-FEG, JEM 2100F. The TEM samples were prepared by dispersing the materials in isopropyl alcohol; these solutions were placed onto a sample holder with a carbon-coated copper grid. After TEM imaging, energy dispersive X-ray spectroscopy (EDS) elemental mapping were performed to evaluate element distribution in the magnetic catalyst.

Powder X-ray diffraction (XRD) patterns were recorded on a Rigaku X-ray diffractometer equipped with a Cu source (λ = 1.541 Å). Data were recorded at 40 kV, 30 mA, in the range 5º≤ 2θ≤ 90º with step size of 0.1º and count time of 2 s per step. Average crystallite sizes of the Fe_3O_4 and TiO_2 were calculated by Scherrer equation [34]. Fe_3O_4 crystallite sizes were calculated from the (311) plane of the spinel reflections, 2θ = 35.3º using the Scherrer equation. For TiO_2, the anatase peak (1 0 1) was used (2θ = 25.5º).

Inductively coupled plasma optical emission spectrometry (ICP-OES) analyses were performed in a Spectro Arcos apparatus. Samples were dissolved in a mixture of sulfuric acid and hydrofluoric acid (3:1) and heated at 100 °C until complete dissolution in a block digester. Fe was analyzed at λ = 259.941 nm and Ti at λ = 334.941 nm.

Particle size and distribution were evaluated using a Microtrac s3000 particle size analyzer. Laser light-scattering measurements were set at 180°. Samples were diluted with water. Ten measurements were made for each sample at 20 seconds intervals. Average sizes were also obtained by SEM and TEM measurements.

4-MAA Degradation

Photochemical degradation experiments were conducted in a lab-scale cylindrical reactor (500 mL) equipped with a cooling system (20 ºC) and O_2 disperser system (350 cm^3 min^{-1}). Samples were irradiated with a 125 W high-pressure mercury lamp, with maximum emission at λ = 254 nm. In the heterogeneous photocatalytic experiments, the same system was used, adding 1.00 g L^{-1} of Fe_3O_4@TiO_2, 0.66 g L^{-1} of TiO_2 or 0.33 g L^{-1} of Fe_3O_4. Catalyst amounts were chosen in order to use Fe_3O_4 and TiO_2 concentrations comparable to those present in the Fe_3O_4@TiO_2 hybrid material.

In ozonation experiments, a tubular reactor of 350 mL was used. Experiments were performed at a constant gas flow (30 L h^{-1}) and constant inlet ozone concentration (10 mg L^{-1}). Ozone concentrations were monitored by a spectrophotometer (Multi Spec1501, Shimadzu), at λ = 254 nm, in a 1.0 cm path length flow cell. Residual gas exhausted from the reactor was decomposed by a KI solution (2%) before releasing to the environment. The pollutant solution was stirred throughout all experiments. In catalytic experiments, 0.10 g L^{-1} of Fe_3O_4@TiO_2, 0.06 g L^{-1} of TiO_2 or 0.03 g L^{-1} of Fe_3O_4 were used. Before O_3 introduction, materials were kept in contact with the pollutant solution for 15 minutes. For comparation, single ozonations (in the absence of the catalyst) were performed under identical experimental conditions.

In all degradation experiments, 4-MAA concentration was 3.0 10^{-4} mol L^{-1} at pH = 3. At convenient reaction times, samples were removed from the reactor, and the catalyst was separated magnetically or by filtration, depending on the material composition, followed by supernatant analysis. Efficiencies of the different catalysts were evaluated by monitoring total organic carbon (TOC) reduction, using a Shimadzu 5000A analyzer [35].

Adsorption of 4-MAA onto the catalysts was examined by stirring 30 mg of the catalyst in 30 mL of the appropriate concentrations of

the pollutant. After equilibration for at least 180 min, the catalyst was filtered. Concentrations of 4-MAA before and after adsorption were measured by HPLC [36].

A commercial permanent neodymium-iron-boron (NdFeB) magnet with size of 10 x 20 x 40 mm was used to separate the magnetic catalyst from the solution. The flux density of the magnet was 500 mT.

Results and Discussion

Preparation and characterization of materials

Particle size is one of the crucial parameters that affect catalysts activity because many of the chemical and physical properties associated with magnetic nanoparticles are strongly dependent upon the particle diameter. The smaller particles are, the larger its surface area per unit volume and, consequently, more active sites are available. Narrower particle distributions improve homogeneity and dispersion properties. Several studies reveal that both particle size and distribution of nanoparticles have a significant effect on the stability of dispersions and their performances as catalysts [4]. The effect of particle size is also important on dispersion of particles in solution, in order to obtain uniform and stable suspensions [37].

Table 2 shows particle size and its respective distribution obtained in different experimental conditions determined by statistical uniform design. Materials with an average size ranging between 11 nm and 35 nm and distributions between 0.23 and 0.77 were obtained.

In order to assess the effect of the variables on particle sizes and respective distributions, results were inserted into the Statistica software. Since there were two response variables, the desirability function was applied, as proposed by Derringer, in order to obtain optimum experimental results [38]. Desirability values scale ranged from 0 (undesirable) to 1 (desirable). The reference values considered desirable were 10 nm (particle size) and 0.20 (distribution). The desirability functions for each variable are depicted in Fig. 1. Temperature, sonication time, precipitation reaction stirring speed and base addition rate were the variables that had a greater effect on particle size. On the other hand, temperature, precipitation reaction stirring time, sonication time and base concentration were the most important parameters that influenced particle size distribution. The observed effects are only valid for experimental conditions evaluated because the statistical design does not allow extrapolation of results. Most of the variables have the same effect on both particle size and distribution. Higher temperature (F1) and stabilizer percentage (F8), as well as longer dispersion stirring time (F6) led to an increase in particle size and distribution. On the other hand, longer sonication time (F3) and higher base concentration (F7) contribute to smaller particle size and distribution.

Table 2. The experimental design matrix with values used for each factor and corresponding results of particle size and distribution.

Experiment	F1	F2	F3	F4	F5	F6	F7	F8	Hydrodynamic diameter (nm)	Distribution
1	10	75	63	400	1.5	9.5	0.775	2.5	11	0.23
2	40	15	45	1200	1.3	10.5	0.475	1.3	35	0.33
3	25	135	57	2000	1.7	5.5	0.625	1.6	17	0.28
4	5	45	39	1600	0.5	4.5	0.550	2.8	27	0.25
5	45	90	51	1100	0.7	2.5	0.925	2.2	16	0.22
6	30	120	27	600	1.1	6.5	0.400	3.4	28	0.77
7	15	105	21	1400	0.9	8.5	0.850	1.0	29	0.25
8	35	60	33	1800	1.9	7.5	1.000	3.1	27	0.30
9	20	30	15	800	2.1	3.5	0.700	1.9	13	0.36

Precipitation reactions stirring time/speed (F2 and F4) and base addition rate (F5) showed an opposite effect in particle size and distribution. For the variable precipitation reaction stirring time, it was observed that longer times favored the formation of particles with smaller size and wider distribution. The contact of stirring paddles with the particles may break large agglomerates. However, this process could lead to the formation of agglomerates with different sizes, which widens distribution. Another variable that showed an opposite effect on the variable-response was precipitation reaction stirring speed. Higher stirring speeds promoted formation of large particles with narrow distributions. Faster agitation favors collision between particles and, depending on the collision energy, agglutination could be favored. On the other hand, as particles agglomerate, size distribution tends to decrease. Base addition rates also showed an opposite effect in the variables response. Higher addition rates favored the formation of particles with smaller size because the base acts as a primary nucleation agent. However, raising base addition rates induces wider particle size distributions. Under the experimental conditions evaluated, different agglomeration nuclei were formed during base addition. Since the total addition times were approximately 1 hour, it is possible that earlier nuclei formation lead to larger agglomerates. Thus, different agglomerate sizes were obtained over the time of base addition.

By statistical modulation, optimal magnetic nanoparticles preparation conditions were: temperature, 5 °C; precipitation reaction stirring time, 30 min; sonication time, 60 min; precipitation reaction stirring speed, 800 rpm; base addition rate, 2.1 mL min^{-1}; dispersion stirring time, 2.5 min; base concentration, 1.0 mol L^{-1}; stabilizer percentage, 1.0%. Under these conditions, Fe_3O_4 magnetic particles with a hydrodynamic diameter of 18 nm and 21% distribution were obtained. Microscopy images (Fig. 2) showed that these agglomerates were formed mostly by spherical particles with diameters in the range 5 to 15 nm; some particles presented a rod-like morphology. Fe_3O_4 mean crystallite size, calculated from XRD data, was ca. 15 nm (Fig. 3). XRD patterns are compatible with magnetite.

This material was used to prepare the hybrid catalyst Fe_3O_4@TiO_2. SEM/TEM analyses of this catalyst (Fig. 2) show particles with a rod-like morphology and size of ca. 18-20 nm. Light and dark lines seen in Figure 2D are formed by contrast between the atoms that make up the surface of the primary particles. The observed regularity in atom distribution reveals that the material is crystalline. Fig. 3 shows X-ray diffractograms of TiO_2 and Fe_3O_4@TiO_2. Anatase and brookite polymorphs coexist in TiO_2. Diffraction peaks assigned to

magnetite, anatase and brookite are present in the hybrid material Fe_3O_4@TiO_2 [39-41]. The mean crystallite size of TiO_2, calculated from the XRD pattern, was 5 nm. No significant variation in the crystallite sizes of magnetite and TiO_2 was observed in the hybrid material Fe_3O_4@TiO_2 (Table 3).

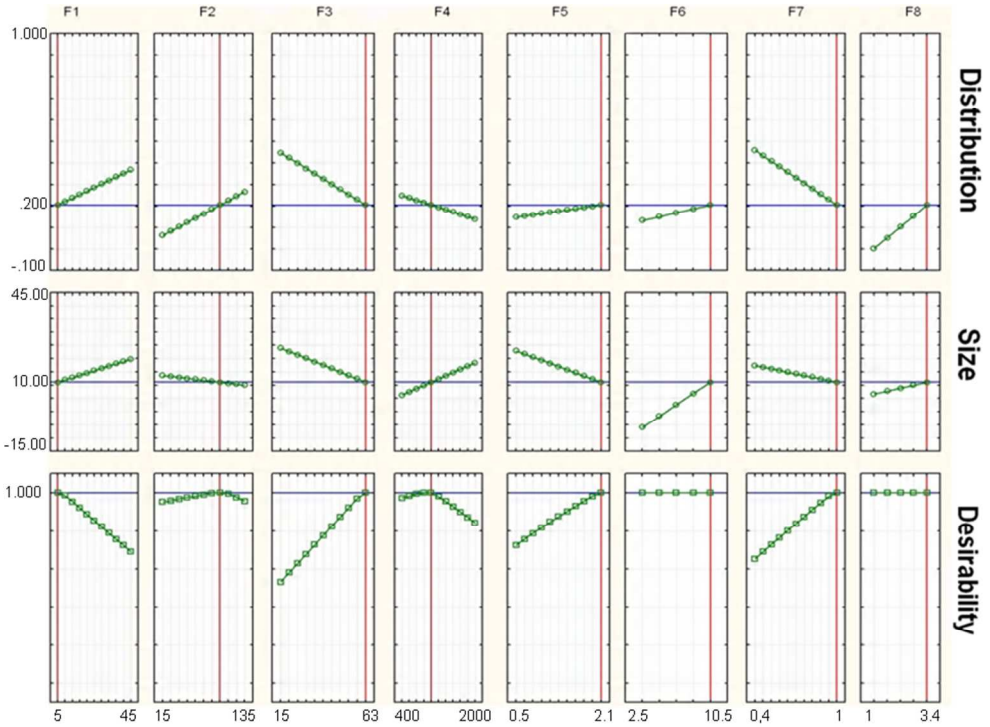

Figure 1. Normalized desirability profiles for the factors studied.

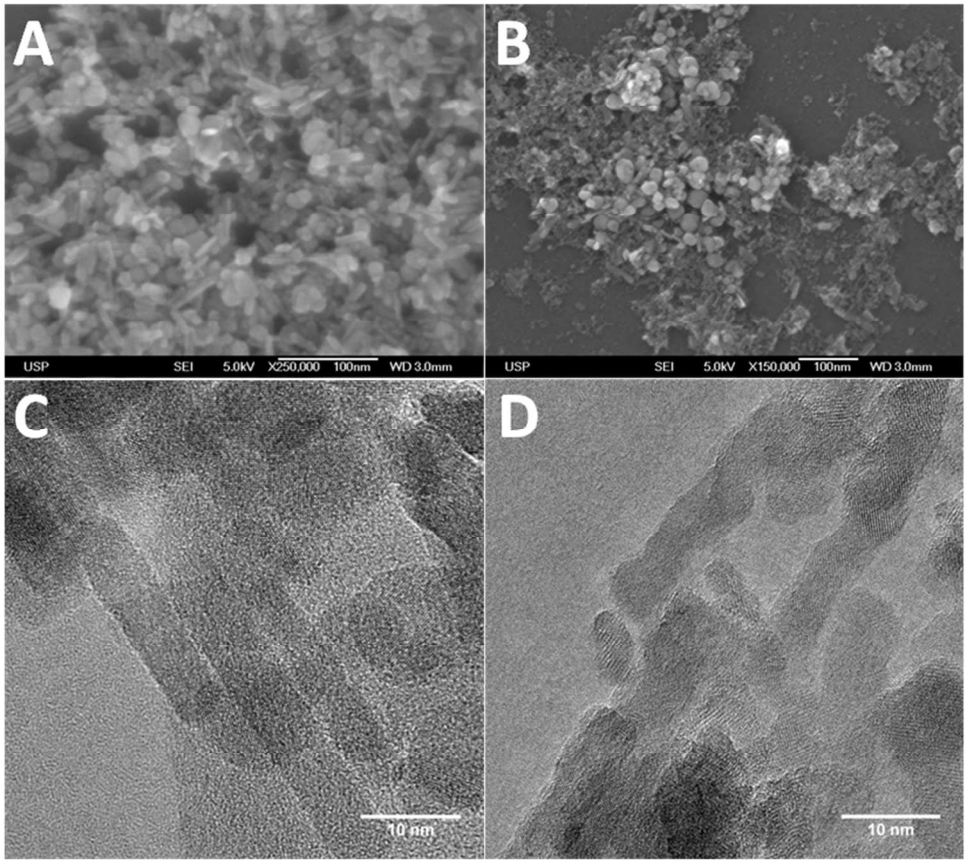

Figure 2. SEM images: A) Fe_3O_4; B) Fe_3O_4@TiO_2. TEM images: C) Fe_3O_4; D) Fe_3O_4@TiO_2.

Journal Name RSCPublishing

ARTICLE

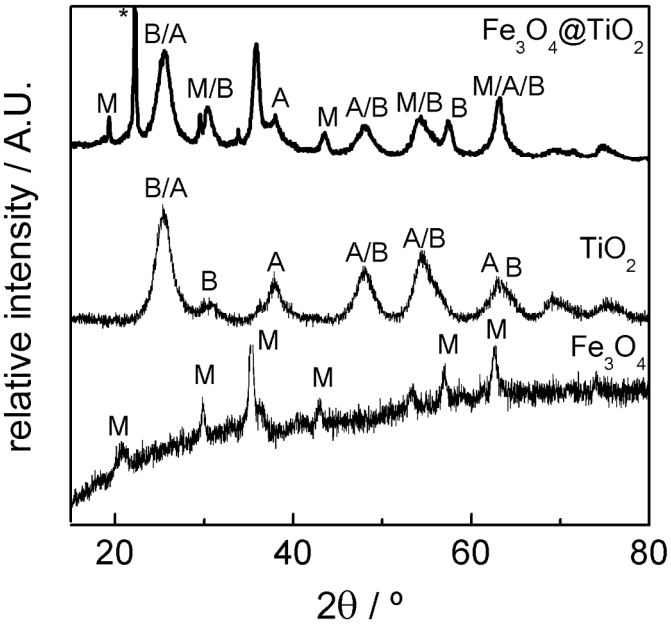

Figure 3. X-ray diffraction pattern of Fe_3O_4, TiO_2 and Fe_3O_4@TiO_2. Asterisk indicates an impurity peak, probably Fe(II)-Fe(III) hydroxychloride. A: anatase; B: brookite; M: magnetite.

Fig. 4 shows thermogravimetric and differential thermoanalysis of Fe_3O_4@TiO_2. Two different stages were observed: dehydration and stabilizer decomposition. The first mass loss event, between 25 and 150 ºC, is related to elimination of water adsorbed on the surface of Fe_3O_4@TiO_2; mass loss was 9% (peak at 65 ºC in DTA curve). The second event, at 150 to 350 ºC, showed an exothermic peak at 279 ºC in the DTA curve. The total mass loss in this step was 33%, which is probably due to the elimination of organic residues from TMA on the catalyst surface. No transition phases were observed in the temperature range evaluated. Based on these results, the materials were submitted to a thermal treatment at 300 ºC for 1 hour.

The Fe_3O_4@TiO_2 catalyst was also analyzed by FTIR in order to verify the presence of magnetite recovered by TiO_2 (Fig. 5). The characteristic band of magnetite, at 560 cm^{-1}, assigned to Fe–O stretching vibrations of the magnetite lattice, was absent in the spectra of Fe_3O_4@TiO_2. In this region, TiO_2 absorbs more than magnetite (due to Ti – O Ti stretching vibrations), thereby covering the magnetite band [22, 42]. The Fe_3O_4@TiO_2 IR spectrum has most of the bands observed in pure TiO_2, which may be indicative of the formation of a hybrid material Fe_3O_4@TiO_2, with TiO_2 in the surface. The presence of water is evidenced by the appearance of the bending mode at 1640 cm^{-1} and the stretching mode at 3400 cm^{-1}. Surface hydroxylation is a favorable characteristic for the catalytic activity of TiO_2 because it provides higher capacity for oxygen/ozone adsorption [43].

Interparticle aggregation state could affect the properties of the final hybrid material. TEM/EDS composition maps (Fig. 6) show that Fe and Ti coexist in the same region. Moreover, the in situ sol-gel TiO_2 nanoparticule preparation within the magnetic matrix has led to well-dispersed TiO_2 nanocrystalline domains over the magnetic support.

The proportion of each oxide in the hybrid catalyst was determined by atomic emission spectrometry (data not shown). These results showed a ratio of 1/2 (Fe_3O_4/TiO_2, m/m), which agrees with the preparation procedure used.

Texture properties of Fe_3O_4, TiO_2, and Fe_3O_4@TiO_2 were measured by N_2 sorption. From the isotherms (data not shown), it was possible to evaluate pore size distribution, pore shape and surface area of the material (Table 3). These parameters are important in the application of this material as a catalyst. Pure TiO_2 physisorption isotherm is classified as type IV with an H2 hysteresis loop, characteristic of ink-bottle mesopores [33, 44]. The N_2 sorption isotherm of Fe_3O_4@TiO_2 also showed a type IV isotherm; however, the hysteresis loop presented a contribution of both H2 and H3 hysteresis type, suggesting the formation of slit shaped pores. Fe_3O_4@TiO_2 exhibited better textural properties than pure TiO_2, showing higher pore volume and specific surface area.

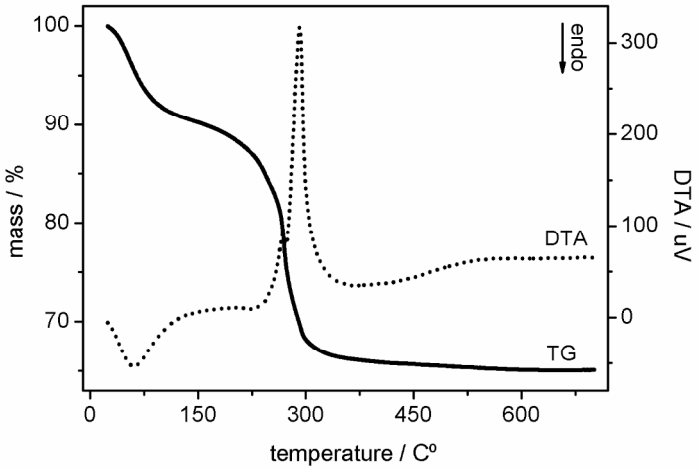

Figure 4. TG/DTA curves of Fe_3O_4@TiO_2.

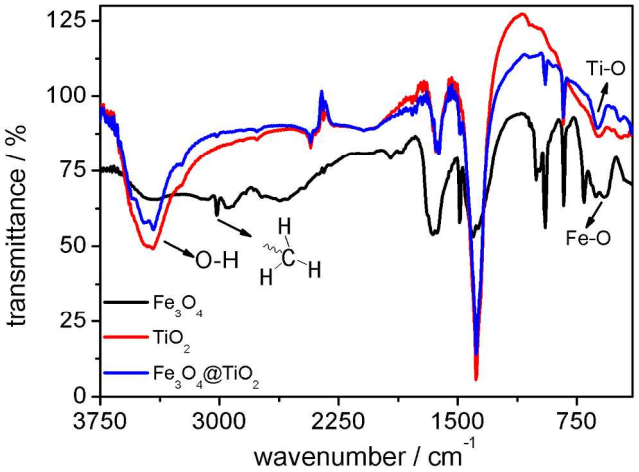

Figure 5. FTIR spectra of Fe_3O_4, TiO_2, and Fe_3O_4@TiO_2.

Degradation tests

The efficiency of the multifunctional catalyst was evaluated in the mineralization degree of 4-MAA by two different oxidative processes (Fig. 7).

The first set of experiments was conducted using the ozonation processes. Comparative experiments were performed to investigate the effect of catalyst on the process efficiency. The experiments were conducted using only ozone (O_3) and heterogeneous catalytic ozonation (O_3/TiO_2, O_3/Fe_3O_4, $O_3/Fe_3O_4+TiO_2$ and $O_3/Fe_3O_4@TiO_2$) processes with pH = 3. Ozone decomposition in water is strongly pH-dependent and is faster with an increase of pH. At low pH, the ozonation reaction is accomplished via direct ozone oxidation [45]. Thus, pH = 3 was chosen to evaluate the capability of the prepared multifunctional catalyst for decomposition of ozone and hydroxyl radicals formation. All ozonation experiments were carried out in absence of UV radiation.

Table 3. Crystallite sizes and texture parameters for Fe_3O_4, TiO_2 and $Fe_3O_4@TiO_2$.

Sample	Pore radius (nm)		Total pore volume ($cm^3\ g^{-1}$)		Specific surface area ($m^2\ g^{-1}$)	Crystallite sizes (nm)	
	DFT	BJH_{ads}	DFT	BJH_{ads}	BET	**Fe_3O_4**	**TiO_2**
Fe_3O_4	5.6	2.5	0.32	0.32	50	15	---
TiO_2	1.8	2.1	0.14	0.13	130	---	5
Fe_3O_4/TiO_2	1.8	1.7	0.18	0.17	175	17	4

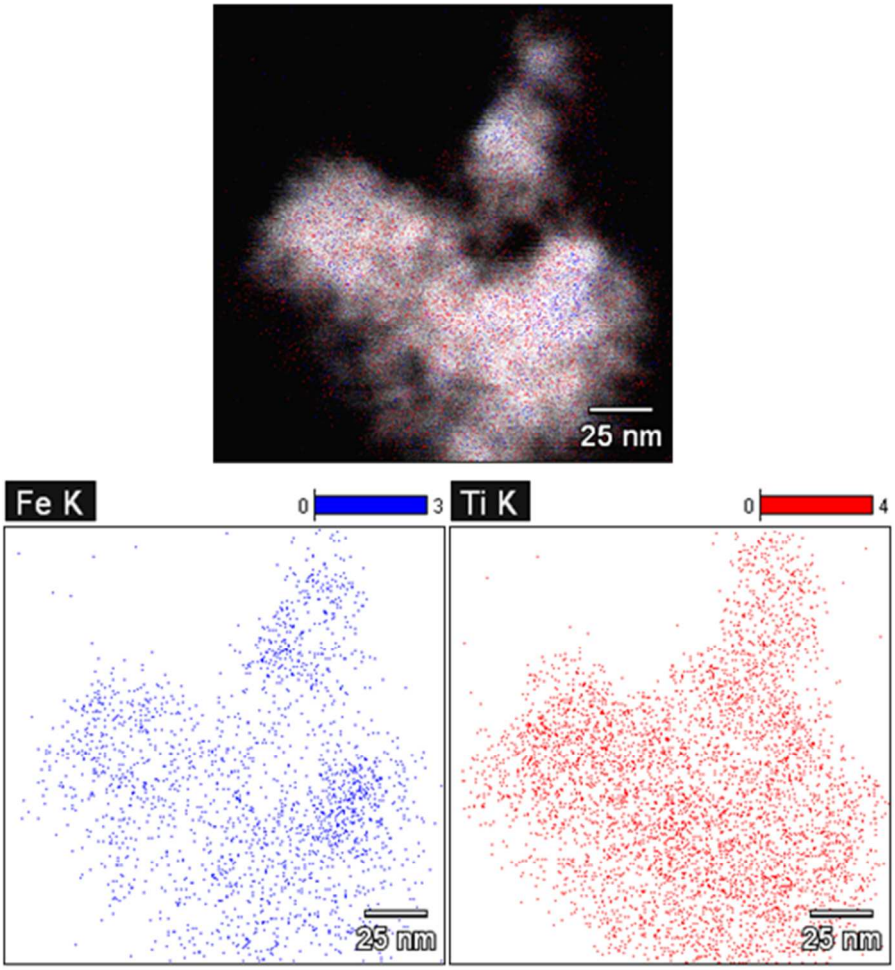

Figure 6. Elemental image composition map of $Fe_3O_4@TiO_2$ (TEM/EDS).

As observed in Fig. 7A, ozone alone (O_3) produced 40% 4-MAA mineralization within 180 minutes of treatment. In the same treatment time, ozonation in the presence of pure TiO_2 (O_3/TiO_2) mineralized the same amount (40%) of the pollutant, which demonstrates that TiO_2 has no activity in the experimental conditions evaluated. The same behavior was observed for ozonation in the presence of Fe_3O_4 (O_3/Fe_3O_4), which also showed no catalytic activity for 4-MAA mineralization. On the other hand, an increase of 50% in the mineralization of the pollutant compound was observed when $Fe_3O_4@TiO_2$ was present during the ozonation process ($O_3/Fe_3O_4@TiO_2$). Using the hybrid catalyst 60% of 4-MAA was mineralized after 180 minutes of treatment. Control adsorption

experiments were carried out. No significant TOC content variation (ca. 4%) was observed without the presence of ozone. So, single adsorption is apparently not sufficient to remove 4-MAA. In addition, no synergistic effect was observed using TiO_2 and Fe_3O_4 simultaneously ($O_3/Fe_3O_4+TiO_2$). In this situation, 4-MAA mineralization was 40% as observed with ozone alone, neat TiO_2 and neat Fe_3O_4 individually.

The Langmuir–Hinshelwood kinetic model was applied to evaluate kinetics of the ozonation processes in the time range between 5 and 180 minutes. 4-MAA mineralization follows a pseudo-first order kinetics [46]. The observed constant (k_{obs}) and half-life ($t_{1/2}$) also reveal a significant effect of Fe_3O_4@TiO_2 on the mineralization of 4-MAA by ozone. k_{obs} and $t_{1/2}$ for the catalyzed process were equal to $5.5x10^{-3}$ min^{-1} and 135 min (R^2 = 0,9967), respectively. Under the same conditions, non-catalyzed processes showed k_{obs} and $t_{1/2}$ of $1.8\ x10^{-3}$ min^{-1} and 470 min (R^2 = 0,9826), respectively.

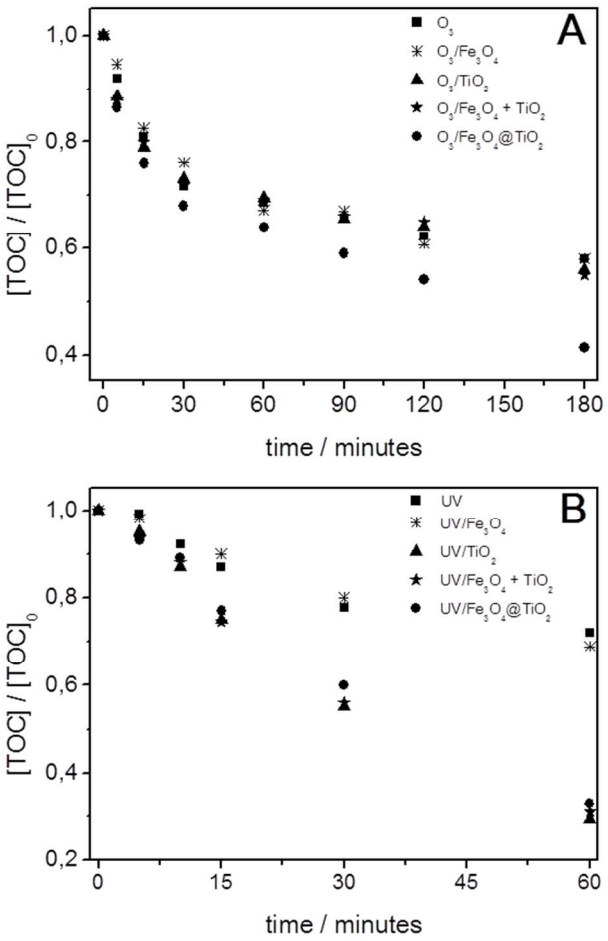

Figure 7. 4-MAA mineralization by different oxidative processes. Experimental conditions: $[4\text{-MAA}]_0 = 3x10^{-4}$ mol L^{-1}; pH = 3. A) ozonation processes. Catalyst loading: Fe_3O_4 = 0.033 g L^{-1}; TiO_2 = 0.066 g L^{-1}; Fe_3O_4@TiO_2 = 0.100 g L^{-1}. B) photochemical processes. Catalyst loading: Fe_3O_4 = 0.33 g L^{-1}; TiO_2 = 0.66 g L^{-1}; Fe_3O_4@TiO_2 = 1.00 g L^{-1}.

Data in literature regarding Fe_3O_4 and TiO_2 show that these materials are proven to be effective in the enhancement of ozonation efficiency [47-51]; however, this effect was not observed under the experimental conditions evaluated in the present study. On the other hand, results showed that the multifunctional catalyst Fe_3O_4@TiO_2 exhibited high catalytic activity.

Preparation procedure and characterization data indicates that the hybrid catalyst surface is mainly composed of TiO_2, well-dispersed and crystalline. Hydroxyl groups are present on TiO_2 surface in water [45]. It is supposed that these hydroxyl groups react with dissolved ozone to generate hydroxyl radicals. Although Fe_3O_4@TiO_2 and pure TiO_2 materials have similar surface composition, their textural properties are distinct. It is well known that the catalyst activity depends on morphology [8, 45, 48]. Fe_3O_4@TiO_2 presented a specific surface area almost 35% larger than pure TiO_2, as shown in Table 3. In addition, the hybrid material also presented higher pore volumes than pure TiO_2 (ca. 30%). Moreover, as discussed before, these materials exhibited different mesoporous structures. The activity of Fe_3O_4@TiO_2 could be attributed to the formation of well-dispersed and crystalline TiO_2 over the magnetic support, with intrinsically distinct mesoporous morphology, as well as higher pore volumes and surface areas than pure TiO_2. Thus, catalyst physical variables have great influence on the catalyst ozonation activity. Indeed, the quantity of 4-MAA adsorbed at the surface of Fe_3O_4@TiO_2 was higher than for pure TiO_2. The amounts of 4-MAA adsorbed in Fe_3O_4@TiO_2 and TiO_2 were $4.0x10^{-5}$ mol g^{-1} and $1.5x10^{-5}$ mol g^{-1}, respectively. The adsorption stage has an important role in the catalytic ozonation process [8, 45, 48]. Reactions occur both on the catalyst surface and in aqueous phase. Reactions on the surface involve several steps, such as adsorption, decomposition reaction of ozone and surface oxidation reactions[8].

An important characteristic of a catalyst, from a practical point of view, is its deactivation or potential reuse. The stability and reusability of Fe_3O_4@TiO_2 were evaluated by the catalytic ozonation of 4-MAA through multiple runs. In the catalyst recycling experiments, six successive ozonation tests were conducted under identical experimental conditions, catalyst loading of 1.00 g L^{-1}, pH 3, 4-MAA concentration of $5x10^{-4}$ mol L^{-1} and reaction time of 180 min. The solid was separated from the reaction mixture by applying a magnetic field, washed several times with water, dried at 60 °C and then reused without any further modifications. Upon application of an external magnetic field, the magnetic catalyst was rapidly separated from solution. Typically, 5 min were necessary to remove all particles. This procedure was chosen to facilitate catalyst recovery and to ensure enough amount of catalyst for further characterization. No relevant adsorption was observed before or after ozonation processes under the evaluated conditions.

As observed in Fig. 8, after 6 times of reuse no significant activity loss was observed, and TOC removal remained consistent throughout all runs, indicating that the catalyst is stable. Besides that, iron amounts in solution were determined by ICP at the end of each experiment. The concentration of leached iron ions was negligible during the ozonation process. Furthermore, the structure of Fe_3O_4@TiO_2 was also probed by XRD after being used six times. No significant difference was observed in the structure. Hence, Fe_3O_4@TiO_2 was proven to be stable and fully recoverable by applying a magnetic field.

It is well known that TiO_2 can decompose a wild range of organic compounds and mineralize them to CO_2 in the presence of UV irradiation [52, 53]. Thus, the application of Fe_3O_4@TiO_2 in the heterogeneous photocatalytic process was also evaluated.

Comparative experiments were performed using single photolysis (UV) and the heterogeneous photochemical processes (UV/TiO2, UV/Fe_3O_4, UV/Fe_3O_4+TiO_2 and UV/Fe_3O_4@TiO_2).

4-MAA photolysis (UV) led to 25% of 4-MAA mineralization after 60 minutes of treatment. In the UV/Fe_3O_4 process, the Fe_3O_4 presence had essentially no contribution to the pollutant

mineralization. On the other hand the photocatalytic process with pure TiO_2 (UV/TiO_2) reached 75% 4-MAA mineralization in the same treatment time. The TiO_2 catalyst increased the efficiency of mineralization by more than 200%, in agreement to other reports in the literature [4, 54]. This high activity could be ascribed to the smaller size of TiO_2 particles. It has been well documented that structural and morphology properties greatly influence activity of TiO_2 nanoparticles, especially those with sizes bellow 10 nm [55]. The photochemical process with neat TiO_2 and Fe_3O_4 (UV/Fe_3O_4+TiO_2) led to the same level of 4-MAA mineralization observed with neat TiO_2 showing no synergistic effect between these two materials if they were in solution in unassociated form.

The Fe_3O_4@TiO_2 hybrid catalyst presented similar 4-MAA mineralization efficiency as pure TiO_2 (70% mineralization in 60 minutes). Thus, the hybrid material reacted like neat TiO_2 in the photocatalytic process; this is an indication that the hybrid material surface was predominantly recovered with TiO_2. Experimental findings indicate that the magnetic core does not influence catalyst activity. This is an interesting behavior, because several studies have reported decreased activity of TiO_2 when coupled to magnetic materials [11, 12, 21]. This activity reduction in hybrid materials usually is due to an unfavorable interaction between electrons in TiO_2 surface and the magnetic core, which leads to an increase in electron-hole recombination.

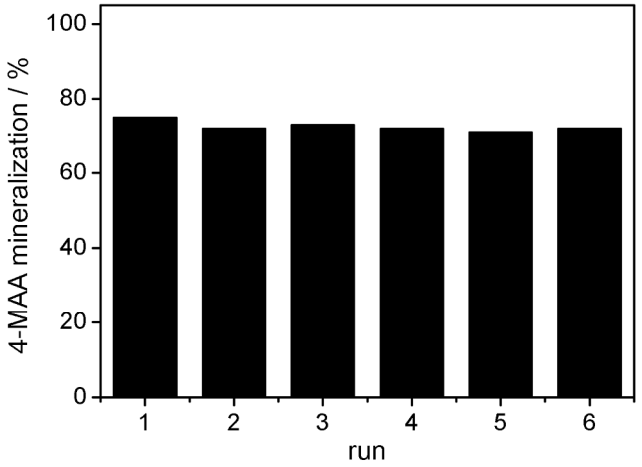

Figure 8. TOC removal during multicycle degradation of 4-MAA by O_3/Fe_3O_4@TiO_2 process. $[4\text{-MAA}]_0$ = $5x10^{-4}$ mol L^{-1}; pH = 3; catalyst loading: Fe_3O_4@TiO_2 = 1.00 g L^{-1}; reaction time = 180 min.

4-MAA mineralization by the photochemical processes also follows a kinetic of pseudo-first order, evaluated in the time range 5 to 60 minutes. For mineralization of 4-MAA by UV/TiO_2, k_{obs} and $t_{1/2}$ were equal to $19.0x10^{-3}$ min^{-1} and 37 min (R^2 = 0.9952), respectively. There was no significant difference in the results for UV/Fe_3O_4@TiO_2 process, with k_{obs} = $17.5x10^{-3}$ min^{-1} and $t_{1/2}$ = 40 min (R^2 = 0.9931). On the other hand, UV and UV/Fe_3O_4 processes showed lower k_{obs} and $t_{1/2}$. For both treatments values were similar: k_{obs} = $6.5x10^{-3}$ min^{-1} and $t_{1/2}$ = 110 min (R^2 = 0.9918) and k_{obs} = $6.2x10^{-3}$ min^{-1} and $t_{1/2}$ = 115 min (R^2 = 0.9896), respectively.

Iron and titanium concentrations were measured after 180 min of UV/Fe_3O_4@TiO_2 process. Titanium concentrations were found to be below the ICP detection limit. On the other hand, iron concentrations in solution were less than 0.01 g L^{-1} which represented 5.0% of the iron content of the fresh catalyst. Comparing ozonation and photochemical processes, it was observed that Fe_3O_4@TiO_2 stability decreased in the presence of UV radiation. For photochemical applications, better stability could be achieved using an insulating layer to prevent iron leaching [12].

Conclusions

Carefully controlled conditions were used to prepare magnetic nanoparticles with controlled size and distribution. The statistical design allowed assessment of the effects of different variables on the desirable properties. Fe_3O_4 nanoparticles were coated by TiO_2 with crystallite sizes around 5 nm. This hybrid multifunctional material was found to be a highly efficient catalyst in the removal of 4-MMA by heterogeneous catalytic ozonation and heterogeneous photocatalysis processes. In the photocatalytic processes, there were no significant differences in the activity of neat TiO_2 compared with Fe_3O_4@TiO_2. On the other hand, in ozonation processes, Fe_3O_4@TiO_2 exhibits considerably improved activity in the mineralization of 4-MAA compared with ozone alone and O_3/TiO_2. Furthermore, the hybrid magnetic catalyst had an excellent long-term stability and could be easily recovered, using an external magnetic field. Results indicate that this material should be a promising catalyst for treatment of wastewater and drinking water.

Acknowledgements

The authors acknowledge Brazilian Research Council (CNPq) and State of São Paulo Research Foundation (FAPESP) for financial support. The authors acknowledge Brazilian Nanotechnology National Laboratory (Campinas, São Paulo), in particular Carlos Kazuo Inoki, for TEM analysis. The authors are grateful to Professor Claudio A. Oller Nascimento, coordinator of Chemical Systems Engineering Center (CESQ/DEQ-EPUSP), and CEPEMA/USP for analytical facilities. The authors also thank Professor Paulo C. Isolani for the English revision.

Notes and references

[a] Instituto de Química, Universidade de São Paulo, CEP 05508-000, São Paulo, Brazil. *e-mail: rsfreire@iq.usp.br
[b] Instituto Federal de Rondônia, CEP 76900-730, Ji-Paraná-RO, Brazil
[c] Departamento de Engenharia Química/Escola Politécnica, Universidade de São Paulo, CEP 05508-900, São Paulo, Brazil.

1. W. Liu, W. Zhong and Y. W. Du, *J. Nanosci. Nanotechnol.*, 2008, **8**, 2781-2792.
2. H. V. Tran, L. D. Tran and T. N. Nguyen, *Mater. Sci. Eng. C*, 2010, **30**, 304-310.
3. M. A. Fox and M. T. Dulay, *Chem. Rev.*, 1993, **93**, 341-357.
4. M. R. Hoffmann, S. T. Martin, W. Choi and D. W. Bahnemann, *Chem. Rev.*, 1995, **95**, 69-96.
5. O. Legrini, E. Oliveros and A. M. Braun, *Chem. Rev.*, 1993, **93**, 671-698.
6. M. I. Litter, Appl. Catal. B: Environ., 1999, **23**, 89-114.
7. T. L. Thompson and J. T. Yates, *Chem. Rev.*, 2006, **106**, 4428-4453.
8. B. Kasprzyk-Hordern, M. Ziólek and J. Nawrocki, *Appl. Catal. B: Environ.*, 2003, **46**, 639-669.
9. A. Mahmoud and R. S. Freire, *Quim. Nova*, 2007, **30**, 198-205.
10. L. S. Soeira and R. S. Freire, in *Catalytic ozonization: a new approach to the treatment of wastewater. Ozone depletion, chemistry and impacts*, ed. S. H. Bakker, Nova Science Publishers Inc., Hauppauge, 2009, pp. 147-162.
11. S. Abramson, L. Srithammavanh, J.-M. Siaugue, O. Horner, X. Xu and V. Cabuil, *J. Nanopart. Res.*, 2009, **11**, 459-465.
12. P. M. Álvarez, J. Jaramillo, F. López-Piñero and P. K. Plucinski, *Appl. Catal. B: Environ.*, 2010, **100**, 338-345.

13. X. W. Lou and L. A. Archer, *Adv. Mat.*, 2008, **20**, 1853-1858.
14. A. V. Pereira, L. Penckowski, M. Vosgerau, M. F. Sassá and O. Fatibello Filho, *Quím. Nova*, 2002, **25**, 553-557.
15. D. F. Feldmann, S. Zuehlke and T. Heberer, *Chemosphere*, 2008, **71**, 1754-1764.
16. H. Ergün, D. A. C. Frattarelli and J. V. Aranda, *J. Pharmaceut. Biomed.*, 2004, **35**, 479-487.
17. M. J. Gómez, C. Sirtori, M. Mezcua, A. R. Fernández-Alba and A. Agüera, *Water Res.*, 2008, **42**, 2698-2706.
18. L. A. Pérez-Estrada, S. Malato, A. Agüera and A. R. Fernández-Alba, *Catal. Today*, 2007, **129**, 207-214.
19. M. J. Gómez, M. J. Martínez Bueno, S. Lacorte, A. R. Fernández-Alba and A. Agüera, *Chemosphere*, 2007, **66**, 993-1002.
20. P. Berger, N. B. Adelman, K. J. Beckman, D. J. Campbell, A. B. Ellis and G. C. Lisensky, *J. Chem. Educ.*, 1999, **76**, 943-948.
21. A. Yanhui, X. Jingjing, F. Degang, B. Long and Y. Chunwei, *Nanotechnology*, 2008, **19**, 405604, pp. 1-6.
22. C. T. Chen and Y. C. Chen, *Anal. Chem.*, 2005, **77**, 5912-5919.
23. Q. He, Z. Zhang, J. Xiong, Y. Xiong and H. Xiao, *Opt. Mater.*, 2008, **31**, 380-384.
24. L. Zhang, W. Wang, L. Zhou, M. Shang and S. Sun, *Appl. Catal. B: Environ.*, 2009, **90**, 458-462.
25. Z. Lu, G. Wang, J. Zhuang and W. Yang, *Colloid Surfaces A*, 2006, **278**, 140-143.
26. Y. Z. Liang, K. T. Fang and Q. S. Xu, *Chemometr. Intell. Lab.*, 2001, **58**, 43-57.
27. Q. S. Xu, Y. Z. Liang and K. T. Fang, *Chemometr. Intell. Lab.*, 2000, **52**, 155-166.
28. J. Jin and H. Guo, *Int. J. Flexible Manuf. Sys.*, 2003, **15**, 167-186.
29. J. Goupy and L. Creighton, *Introduction to Design of Experiments*, Third Edition ed., SAS Institute Inc, 2007.
30. M. R. Mohammadi, D. J. Fray and A. Mohammadi, *Micropor. Mesopor. Mat.*, 2008, **112**, 392-402.
31. S. Brunauer, P. H. Emmett and E. Teller, *J. Am. Chem. Soc*., 1938, **60**, 309-319.
32. E. P. Barrett, L. G. Joyner and P. P. Halenda, *J. Am. Chem. Soc.*, 1951, **73**, 373-380.
33. S. Lowell, J. E. Shields, M. A. Thomas and M. Thommes, *Characterization of Porous Solids and Powders: Surface Area, Pore Size and Density*, Kluwer Academic Publishers, Dordrecht, 2004.
34. M. T. Weller, *Inorganic Materials Chemistry*, Oxford University Press Inc., New York, 1994.
35. Standard Methods for the Examination of Water and Wastewater, 20th ed., in American Public Health Association (APHA), The American Water Works Association (AWWA), Water Environment Federation (WEF), 2003.
36. H. Z. Senyuva, I. Aksahin, S. Ozcan and B. V. Kabasakal, *Anal. Chim. Acta*, 2005, **547**, 73-77.
37. D. Peddis, C. Cannas, A. Musinu and G. Piccaluga, *Chem. Eur. J.*, 2009, **15**, 7822-7829.
38. G. Derringer and R. Suich, *J. Qual. Technol.*, 1980, **12**, 214-219.
39. J. P. Jolivet, C. Chaneac and E. Tronc, *Chem. Commun.*, 2004, 481-483.
40. S. K. Kwon, K. Shinoda, S. Suzuki and Y. Waseda, *Corros. Sci.*, 2007, **49**, 1513-1526.
41. P. H. Refait, M. Abdelmoula and J. M. R. Génin, *Corros. Sci.*, 1998, **40**, 1547-1560.
42. Z. G. Peng, K. Hidajat and M. S. Uddin, *J. Colloid Interf. Sci.*, 2004, **271**, 277-283.
43. M. Ye, Q. Zhang, Y. Hu, J. Ge, Z. Lu, L. He, Z. Chen and Y. Yin, *Chem. Eur. J.*, 2010, **16**, 6243-6250.
44. K. S. W. Sing, *Pure Appl. Chem.*, 1982, **54**, 2201-2218.
45. J. Nawrocki and B. Kasprzyk-Hordern, *Appl. Catal. B: Environ.*, 2010, **99**, 27-42.
46. B. Liu, X. Zhao, C. Terashima, A. Fujishima and K. Nakata, *Phys. Chem. Chem. Phys.*, 2014, **16**, 8751-8760.
47. X. Mou, X. Wei, Y. Li and W. Shen, *CrystEngComm*, 2012, **14**, 5107-5120.
48. F. J. Beltrán, F. J. Rivas and R. Montero-de-Espinosa, *Appl. Catal. B: Environ.*, 2002, **39**, 221-231.
49. R. Gracia, S. Cortes, J. Sarasa, P. Ormad and J. L. Ovelleiro, *Water Res.*, 2000, **34**, 1525-1532.
50. L. Mansouri, M. Sabelfeld, S.-U. Geissen and L. Bousselmi, *Desalination Water Treat.*, 2013, 1-12.
51. G. Moussavi, R. Khosravi and N. R. Omran, *Appl. Catal. A: Gen.*, 2012, **445-446**, 42-49.
52. F. Fresno, R. Portela, S. Suárez and J. M. Coronado, *J. Mater. Chem. A*, 2014, **2**, 2863-2884.
53. S.-Q. Liu, *Environ. Chem. Lett.*, 2012, **10**, 209-216.
54. D. Kanakaraju, B. Glass and M. Oelgemöller, *Environ. Chem. Lett.*, 2014, **12**, 27-47.
55. S. Y. Chae, M. K. Park, S. K. Lee, T. Y. Kim, S. K. Kim and W. I. Lee, *Chem. Mater.*, 2003, **15**, 3326-3331.